

SUPPORTING INFORMATION

Supporting Information

Cultivating Crystal Lattice Distortion in IrO₂ via Coupling with MnO₂ to Boost Oxygen Evolution Reaction with High Intrinsic Activity

Table of Contents

Experimental Procedures	4
Scheme S1. Synthesis of Ir/Mn composites.....	8
Figures	9
Fig S1. The Iridium demand by electrochemical application and its proportion to the total demand in recent years.....	9
Fig S2. The forming sequence of IrO ₂ and δ-MnO ₂ revealed by ICP analysis	10
Fig S3. EDS spectra of the composites.	11
Fig S4. SEM images of the composites.	12
Fig S5. SEM image of δ-MnO ₂	13
Fig S6. SEM image of a contrast sample.	14
Fig S7. Element distribution of the Ir _{0.4} /Mn _{0.6}	15
Fig S8. HRTEM images for Ir _{0.3} /Mn _{0.7}	16
Fig S9. XRD pattern of the hydrothermally prepared MnO ₂	17
Fig S10. Brunauer-Emmett-Teller (BET) of commercial IrO ₂	18
Fig S11. BET analysis of the Ir/Mn composites.....	19
Fig S12. Pore volume distribution of the Ir/Mn composites.	20
Fig S13. The electrochemical impedance spectroscopy (EIS) of the Ir/Mn composites.	21
Fig S14. Fit of the EIS curves of Ir/Mn composites.....	22
Fig S15. Electrochemical analysis of the composites.....	23
Supplementary Note S1. The mechanism of OER in acid	23
Fig S16. Normalized cyclic voltammogram curves.	25
Fig S17. The cyclic voltammogram curves with different scan rates.	26
Fig S18. The oxide specific activity normalized to electrochemical surface area of Ir _{0.4} /Mn _{0.6} and IrO ₂ in acidic electrolyte.	27
Fig S19. Comparison of the Ir 4f peak intensity of IrO ₂ and Ir _{0.3} /Mn _{0.7}	28
Fig S20. Mn2p spectra of Ir _{0.3} /Mn _{0.7} and δ-MnO ₂	29
Fig S21. Ir4f and Mn3s spectra of Ir _{0.3} /Mn _{0.7}	30
Fig S22. O1s XPS spectra of δ-MnO ₂ , IrO ₂ , and Ir _{0.3} /Mn _{0.7}	31
Supplementary Note S2. The discussion on XPS	31
Fig S23. The k ₂ -weighted Ir-L _{III} edge EXAFS spectra.	33
Fig S24. XAS analysis of Mn.	34

SUPPORTING INFORMATION

Fig S25. Second order derivative of Ir L _{III} edge of IrO ₂ and Ir/Mn composites.	35
Tables	36
Table S1. The precursors during preparation of Ir/Mn catalysts.	36
Table S2. EIS fit parameters for Ir/Mn composites in Fig S14.	37
Table S3. The electrochemical performance comparison of Ir _{0.4} /Mn _{0.6} against other Ir/Mn catalysts.	38
Table S4. The electrochemical performance comparison of Ir _{0.4} /Mn _{0.6} against other Ir oxide-based catalysts.	39
Table S5. Crystal structure change of IrO ₂ in the composites simulated by Diamond software.	40
Supplementary Note S3. Discussion on simulation by Diamond	40
References	41

Experimental Procedures

The chemicals are of analytical grade and were used as received without further purification.

Synthesis of IrO₂, MnO₂ and Ir/Mn composites: The different ratios between Ir and Mn were achieved by varying the concentration of the Ir or Mn precursor. In a typical procedure, 113.4 mmol L⁻¹ Mn(NO₃)₂ and 56.7 mmol L⁻¹ H₂IrCl₄ with required amount were mixed in 50mL autoclave, and kept 5min for peroxidation of Mn after addition of 500uL 30% H₂O₂. Then 15mL 0.66M NaOH was added, resulting in drastic decomposition of H₂O₂ and successive formation of indissoluble solid. The mixture was aged for 10min. No surfactant was added in this system to gain greener synthesis approach. The autoclave was sealed tightly and slowly heated in an oven to 220°C. The solution was kept for 12 hours to gain fine crystals, and then naturally cooled down to room temperature. The precipitate was collected, suction filtered and washed several times with deionized water to remove residual ions. The retentate on the filter was dried for dehydration in an oven at 80°C for 1h. The final sample was collected and annealed at 400°C for 6 h to produce excellent crystallinity. As for IrO₂, the synthetic procedure is similar with the preparation of Ir/Mn composite. The only difference is that no Mn precursor is added. As for MnO₂, the synthetic procedure is similar with the preparation of Ir/Mn composite with the only difference being no Ir precursor added.

The synthesis of Ir/Mn composites can be explained by a two-step reaction. Mn(OH)₂ is formed in the first step by reaction of Mn²⁺ with OH⁻, and is oxidized by H₂O₂ to birnessite in the subsequent step. Insertion of cations and H₂O molecules into the interlayers accompanies oxidation of Mn²⁺ to higher valence state.

Insight of synthesis procedure with help of Inductively Coupled Plasma Atomic Emission Spectrometer (ICP-AES) Experiments: Before the hydrothermal synthesis of the Ir_{0.3}/Mn_{0.7} composite, the Mn precursor and Ir precursor were firstly mixed with H₂O₂. Then solution was added with 15mL 0.66M NaOH and kept for 10min before sampling for ICP analysis (step1 in Fig S2). After that, the mixture was aged for another 12 hours (step2 in Fig S2). This step is similar to synthesis of birnessite manganese oxide which has been reported previously.¹ Then the mixture was transferred to an autoclave and hydrothermally heated at 80°C for 8 hours (step3 in Fig S2). Finally, the mixture was kept in the hydrothermal system at 220°C for another 12 hours (t_{final}). Every ICP sample was extracted from supernatant, and the

SUPPORTING INFORMATION

pH was adjusted to acid with 0.1M HCl solution. Actually, IrO₂ precipitated at 220°C, not at 80 °C. We take 80°C into consideration here to describe the forming sequence of IrO₂ and MnO₂.

Electrode preparation: To prepare the working electrode, catalyst inks were deposited on Ti plates. The catalysts (weighted at 6.0mg) were ultrasonically dispersed in 1.5 mL isopropanol / deionized water (2:1 v/v) with 15uL 5% Nafion solution as solvent. The Ti plates (5mm×15mm) were used as supports and pre-cleaned by etching in 10wt % faint boiling oxalic acid for 2 h. Then 7.5uL of each catalyst ink was taken and drop-cast onto the pre-cleaned Ti plate. The catalyst layer on the Ti plate was dried at 60°C for 10min. The process was repeated five times, leading to the total loading at 0.2mg cm⁻². A saturated calomel electrode (SCE) electrode and a polished Pt foil were used as the reference electrode and counter electrode, respectively.

Electrocatalytic Study: The OER performance of the composite materials was investigated by using electrochemical techniques since oxygen evolution behavior is directly proportional to electrons transference. The electrolyte (0.1 M HClO₄) was prepared by dilution of 70% perchloric acid with DI water. Electrocatalytic measurements were carried out with a standard three-electrode electrochemical cell controlled by a CHI660E workstation. As no rotation applied, the O₂ bubble nucleation generated from OER process may partly cover the electrode active surface. At the beginning of the electrocatalytic study, the electrodes were cycled between -0.2 and 1.4 V (vs. SCE) at a scan rate of 50 mV s⁻¹ until the curve values reached stable, leading to steady surface conditions. The polarization curves were obtained by extending the potential up-limit to 1.4V (vs. SCE) scanning at a rate of 10mV s⁻¹. The Tafel plots were got from the staircase voltammetry measurements, in which the potential was progressively elevated by 10 mV steps, and each step was kept for 100 s. As the current values were read at the end of each step, the effect of capacitive current was effectively eliminated. The Ir loading in the IrO₂/MnO₂ composites are based on the Ir/Mn atomic ratios.

For catalysts with porous or layered morphology, the intrinsic electrocatalytic ability should take surface area into consideration, as the active sites are extensively exposed. The electrochemical surface area (ECSA) is proportional to the active sites involved in electrochemical reactions, thus generally considered to be a significant parameter for the high OER performance. Here, the cyclic voltammograms (CVs) were carried out to determine the ECSA by measuring the charging currents of double-layer capacitance at different scan rates. For CVs within 0.1-1.4 V_{RHE}, the curves in some potential regions show oxidation/reduction peaks, which are mainly Faradaic currents (*i_F*) for the change of Ir or Mn oxidation states. The flat parts with no distinct peaks are contributed from the charging currents (*i_c*). To investigate

SUPPORTING INFORMATION

the CVs at low Faradaic current contribution, CVs were additionally recorded for Ir_{0.4}/Mn_{0.6} and IrO₂ between 1.1 V and 1.4 V (vs. RHE) with scan rates of 10, 20, 40, 60, and 80 mV s⁻¹.

To investigate the CVs at low mass transfer resistance, the electrochemical impedance spectroscopy (EIS) measurements were performed in a three-electrode electrochemical cell in a rotating-disc electrode (RDE) configuration. The potential was set at 1.25V vs. SCE (1.49 V vs. RHE), with range of frequency set as 0.1 – 10⁵ Hz and applying the amplitude of 10 mV RMS. To simulate the equivalent resistances and capacitance, impedance data were fitted, and real (Z') and imaginary (Z'') components in the Nyquist plot were analyzed using Zview software (Scribner Associates Inc.). To adjust the RDE system, the working electrode is a little different, and catalysts were deposited on glassy carbon (surface area of 0.196 cm²). The electrodes were kept for 100 s at the set potential to establish stable current response before recording each spectrum.

The electrode potential was converted from the SCE scale to the reversible hydrogen electrode (RHE) scale by following calibration:

$$E \text{ (RHE)} = E \text{ (vs. SCE)} + 0.2415 + 0.0596\text{pH} - iR \quad (1)$$

where i is the current at the applied potential, and R is the uncompensated Ohmic electrolyte resistance measured by electrochemical workstation. The over-potential values (η) were obtained using the following equation:

$$\eta = E \text{ (RHE)} - 1.229\text{V} \quad (2)$$

The values of mass activity (A g⁻¹) and turnover frequency (TOF, s⁻¹) were calculated, and calculation details are as follows:

$$\text{Mass activity} = j/m \quad (3)$$

$$\text{TOF} = (j \times S) / (4 \times F \times n) \quad (4)$$

Here, j is the average current density at a given potential, m is the Iridium loading (for IrO₂ is 0.857 × 0.2 mg cm⁻²) of the electrode. S is the geometric area of the working electrode (0.25cm²), the number 4 represents the electrons transfer in oxygen molecule generation, F means Faraday's constant (96485 C mol⁻¹), and n is the moles of coated Iridium atoms. This calculation assumes that every Iridium atom (rather than Mn) is involved in oxygen evolution.

In the measurement of ECSA, the CVs were carried out in a potential range where no Faradaic processes take place at scan rates ranging from 10 to 80 mV s⁻¹. In this way, the measured currents were mainly contributed by charging current (i_c). The charging currents show linear relationship with the scan rates:

$$i_c = C_d v \quad (5)$$

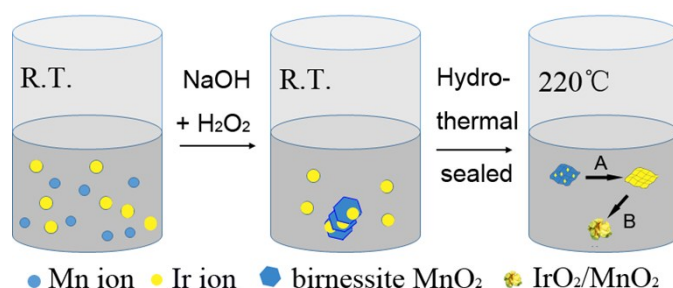
SUPPORTING INFORMATION

in which C_d is capacitance of the double layer and v is the applied scan rate. So one can estimate the ECSA using the following equation:

$$e\text{-ECSA} = C_d/C_s \quad (6)$$

in which the C_s is the specific capacitance of an electrode. For estimation of surface area here, we use general specific capacitances of $C_s = 0.035 \text{ mF cm}^{-2}$.

SUPPORTING INFORMATION



Scheme S1. Synthesis of Ir/Mn composites.

The layered birnessite MnO₂ is formed at room temperature (R.T.), and IrO₂ is formed in hydrothermal reaction. The process A and B are suppositional processes during hydrothermal reaction. A: anchoring and growing of the Ir oxide; B: twisting of the nano-plates.

ACKNOWLEDGMENT

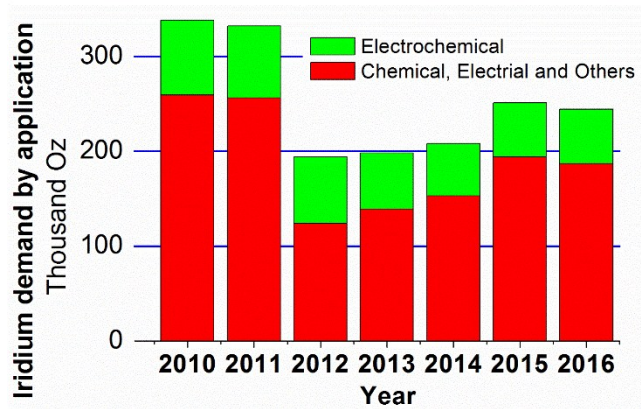
This research is based on the work supported by the National Natural Science Foundation of China (51778229) and the “Shu Guang” project of the Shanghai Municipal Education Commission. We thank beamline BL14W1 (Shanghai Synchrotron Radiation Facility, Shanghai) and Catalysis and Surface Science Endstation (National Synchrotron Radiation Laboratory, Hefei) for providing the beam time.

SUPPORTING INFORMATION

Figures

Fig S1. The Iridium demand by electrochemical application and its proportion to the total demand in recent years.

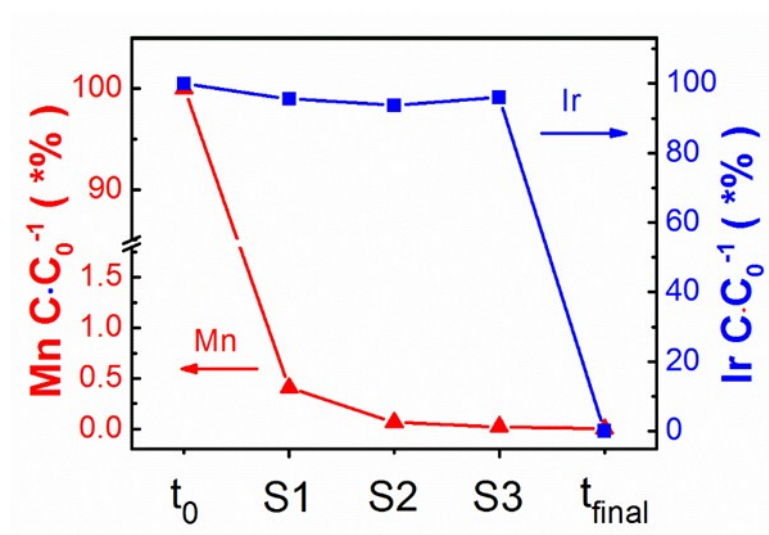
The data are from Platinum group metals (PGM) market reports from Johnson Matthey.^{2, 3}



SUPPORTING INFORMATION

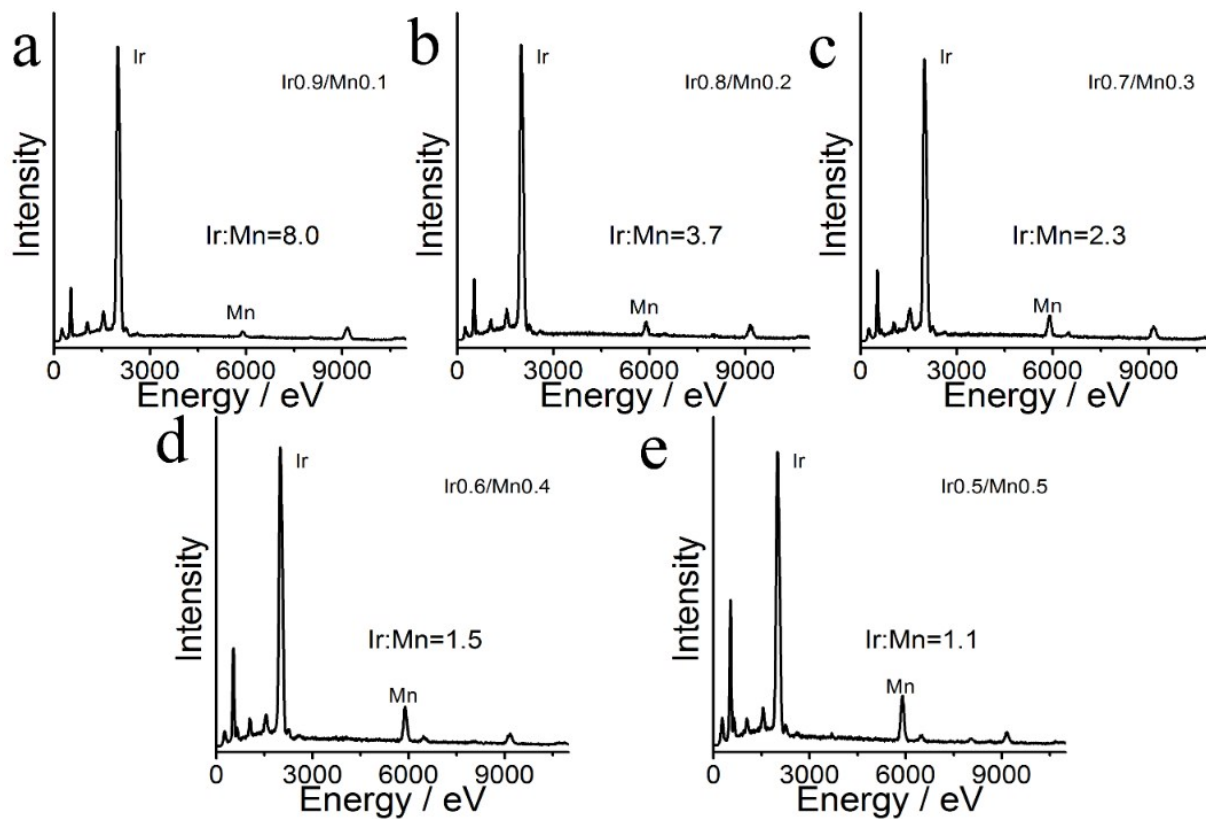
Fig S2. The forming sequence of IrO₂ and δ-MnO₂ revealed by ICP analysis

Firstly the Mn precursor and Ir precursor were mixed with H₂O₂ (t₀). Then solution was added with 15mL 0.66M NaOH. The solution was kept for 10min before sampling for ICP analysis (S1 in Fig. S2 for treatment step1). After that, the mixture was aged for another 12 hours (S2). Then the mixture was transferred to an autoclave and hydrothermally heated at 80°C for 8 hours (S3). Finally, the mixture was kept in hydrothermal system at 220°C for another 12hours (t_{final}). Note that, treatment step3 (S3) at 80°C is applied to further prove that the formation of Ir oxide lags behind, though the synthesis approach of the catalysts does not involve this step. Here, C₀ represents the initial concentration of Mn or Ir.



SUPPORTING INFORMATION

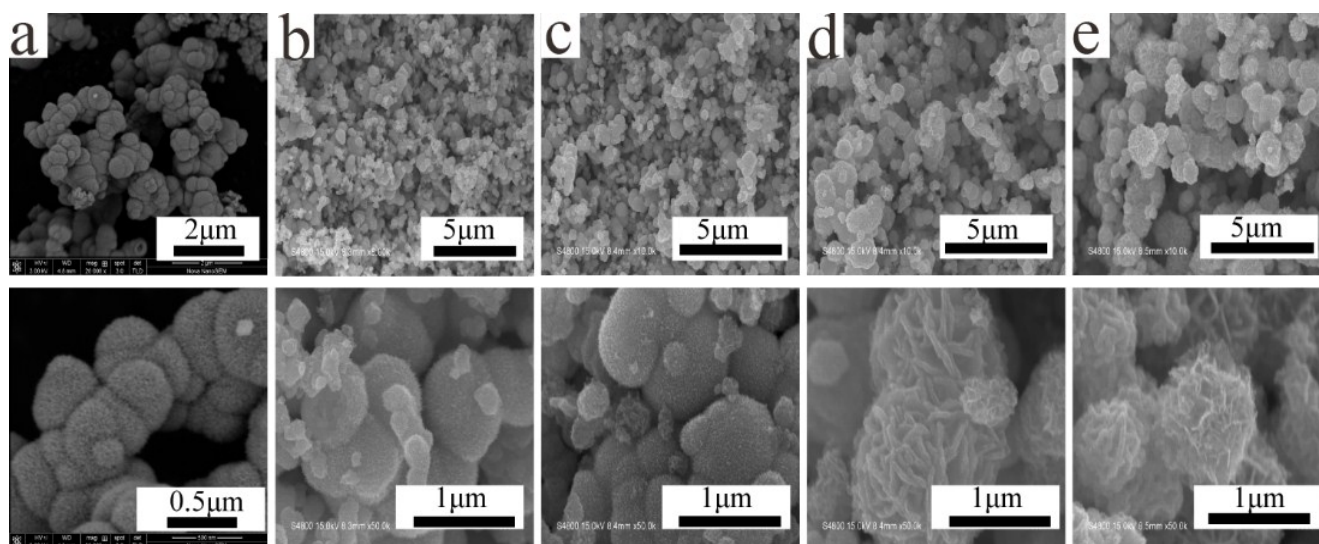
Fig S3. EDS spectra of the composites.



SUPPORTING INFORMATION

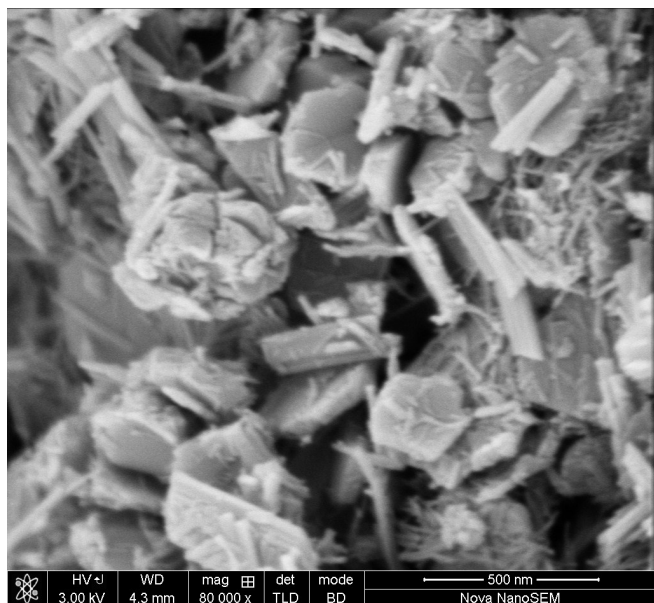
Fig S4. SEM images of the composites.

(a) IrO₂, (b) Ir_{0.9}/Mn_{0.1}, (c) Ir_{0.8}/Mn_{0.2}, (d) Ir_{0.7}/Mn_{0.4}, (e) Ir_{0.4}/Mn_{0.6}.



SUPPORTING INFORMATION

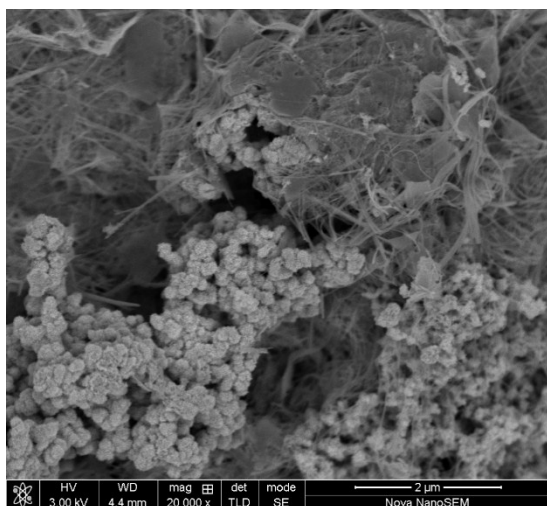
Fig S5. SEM image of δ -MnO₂.



SUPPORTING INFORMATION

Fig S6. SEM image of a contrast sample.

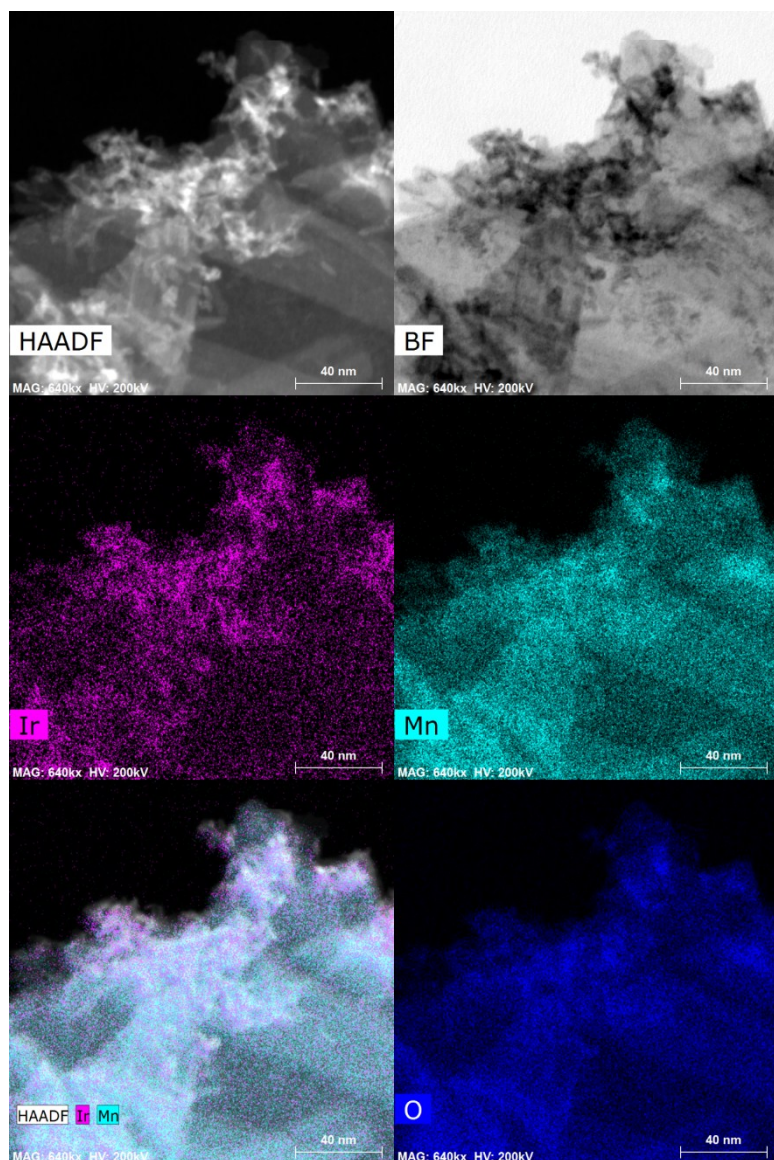
The sample (Ir:Mn=3:7, molar ratio) was prepared following the similar procedure to the Ir/Mn composites, but the Ir precursor was added after birnessite had been generated at room temperature firstly. The SEM image shows inhomogeneous distribution of layered MnO_2 and IrO_2 particles.



SUPPORTING INFORMATION

Fig S7. Element distribution of the Ir_{0.4}/Mn_{0.6}.

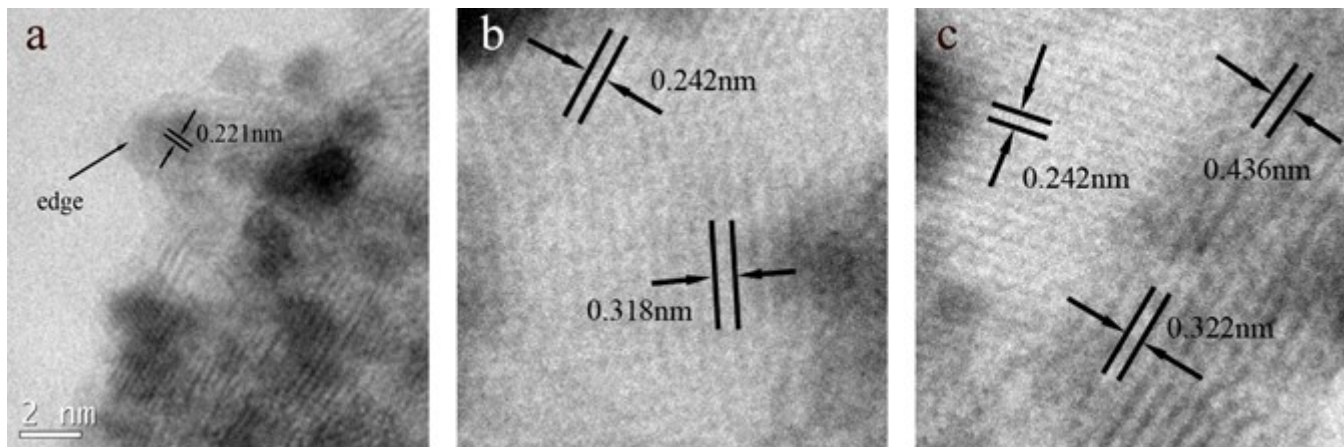
HAADF image is the High-angle annular dark-field. BF is bright field image. The rest images are the EDS mapping of Ir, Mn and O elements.



SUPPORTING INFORMATION

Fig S8. HRTEM images for Ir_{0.3}/Mn_{0.7}.

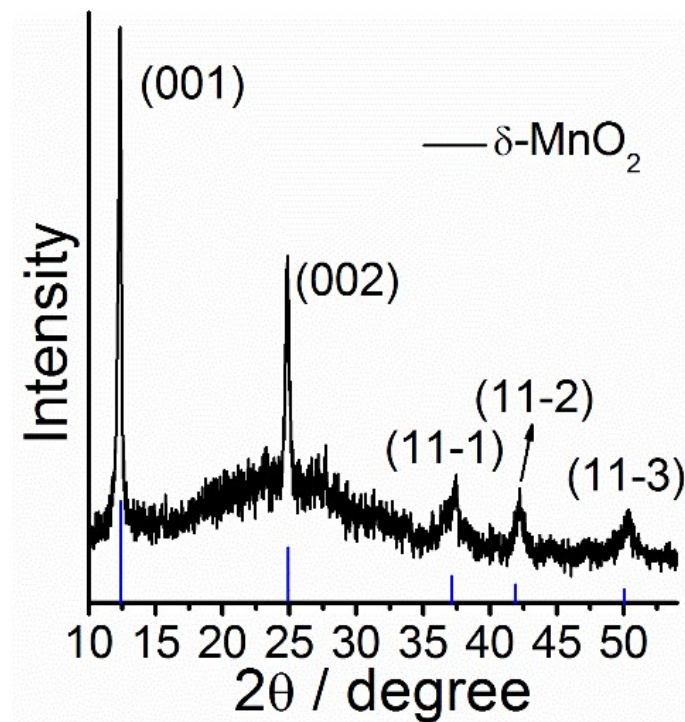
The images show the spatial relation of IrO₂ and Mn oxide. a) The edge of catalyst show amorphous state, b) and c) adjoining parts of MnO₂ and IrO₂. The d-spacing of ~0.24nm belongs to δ -MnO₂ (11-1), and ~0.32nm belongs to IrO₂ (110).



SUPPORTING INFORMATION

Fig S9. XRD pattern of the hydrothermally prepared MnO_2 .

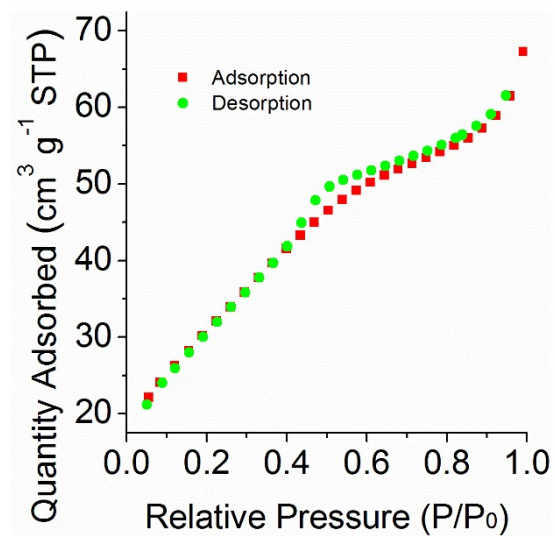
The blue lines show the main peaks of birnessite $\text{Na}_{0.55}\text{Mn}_2\text{O}_4 \cdot 1.5\text{H}_2\text{O}$ (PDF 43-1456).



SUPPORTING INFORMATION

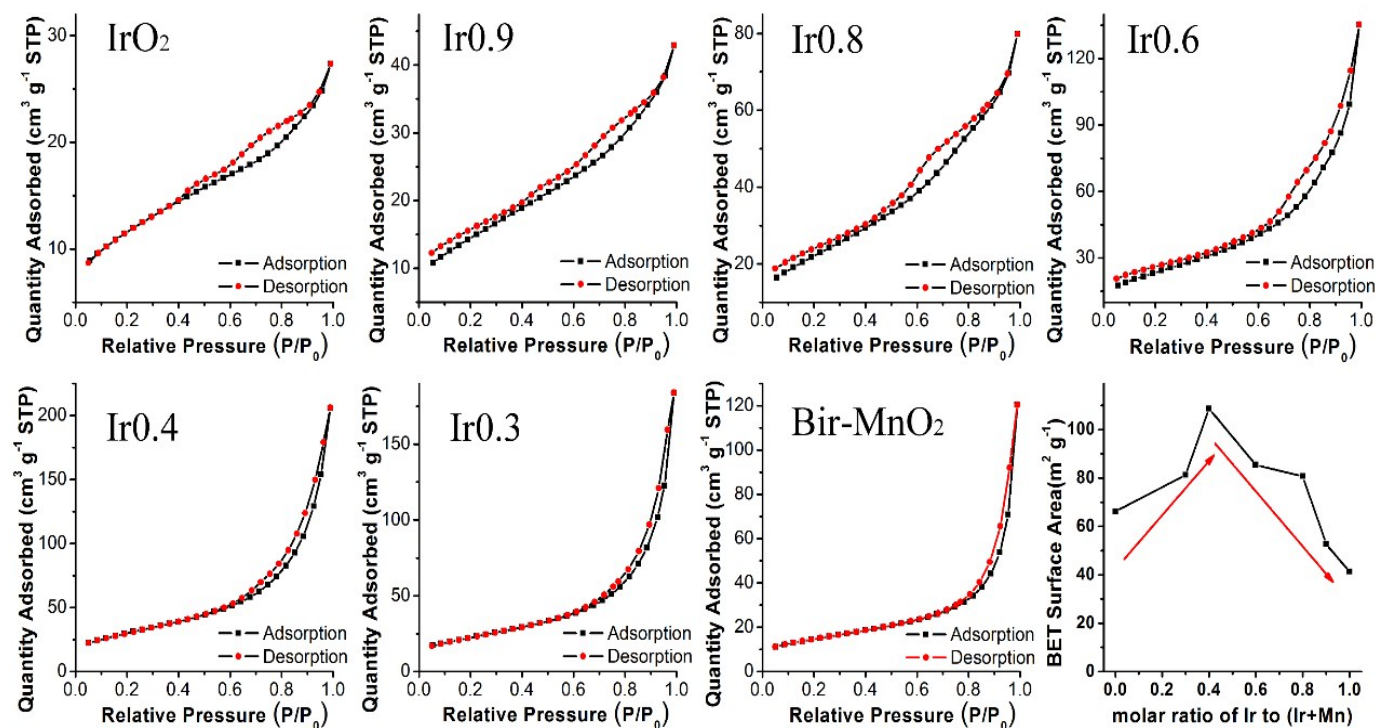
Fig S10. Brunauer-Emmett-Teller (BET) of commercial IrO₂.

The BET surface area is 114.3m² g⁻¹.



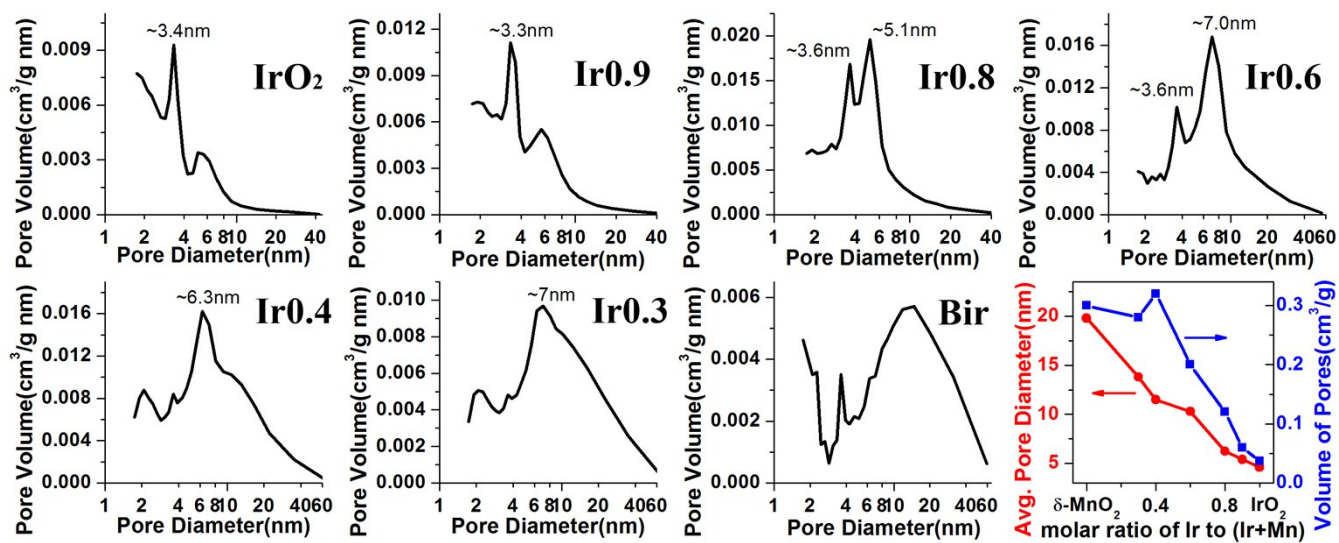
SUPPORTING INFORMATION

Fig S11. BET analysis of the Ir/Mn composites.



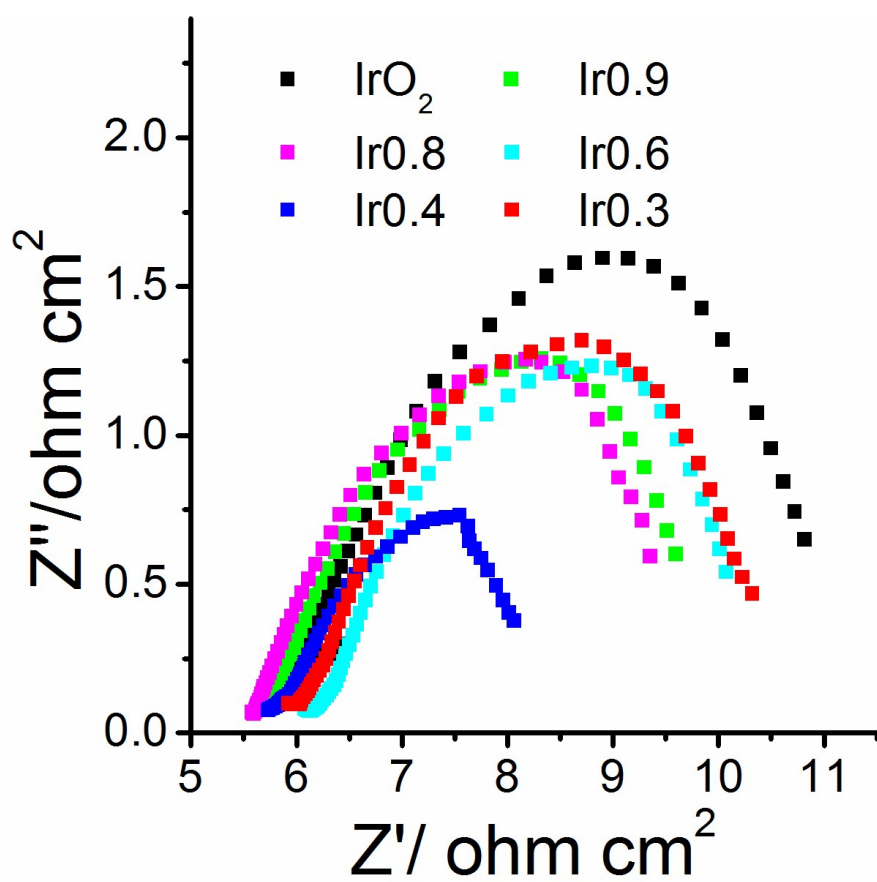
SUPPORTING INFORMATION

Fig S12. Pore volume distribution of the Ir/Mn composites.



SUPPORTING INFORMATION

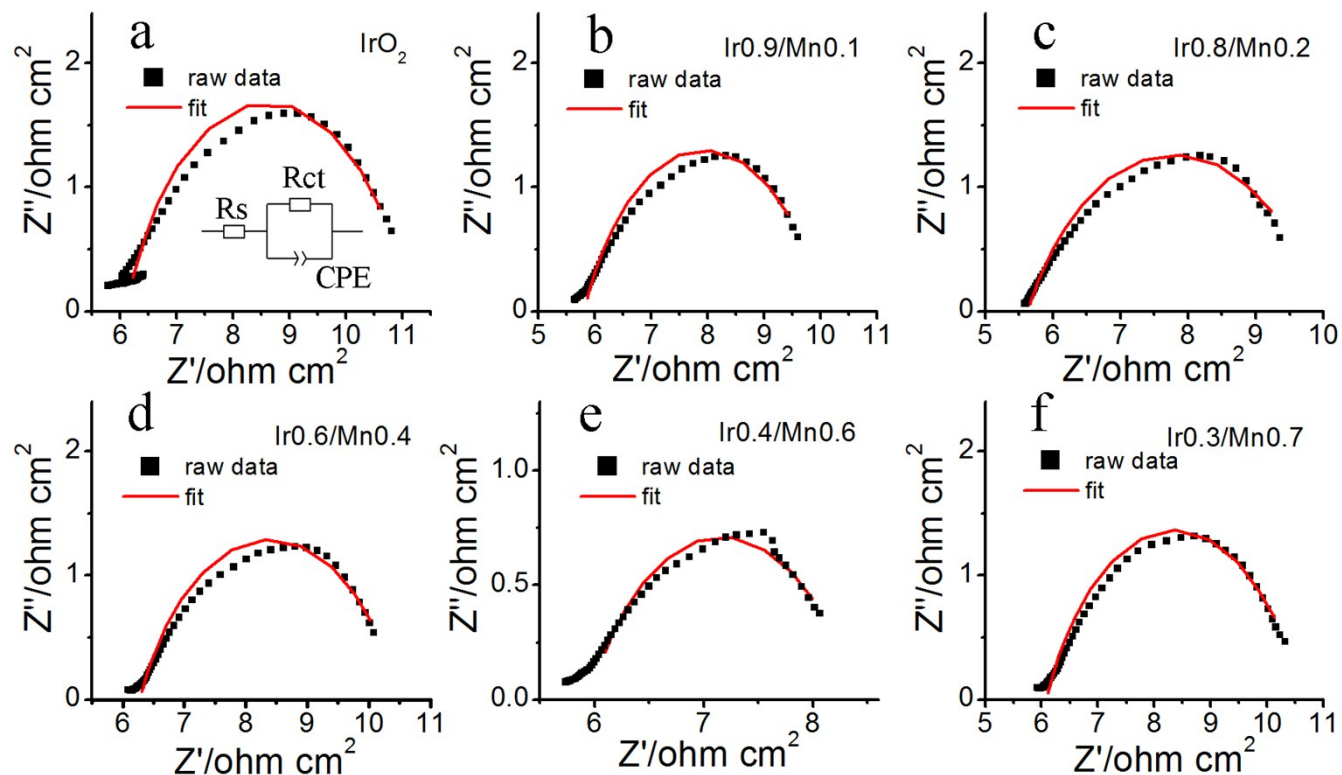
Fig S13. The electrochemical impedance spectroscopy (EIS) of the Ir/Mn composites.



SUPPORTING INFORMATION

Fig S14. Fit of the EIS curves of Ir/Mn composites.

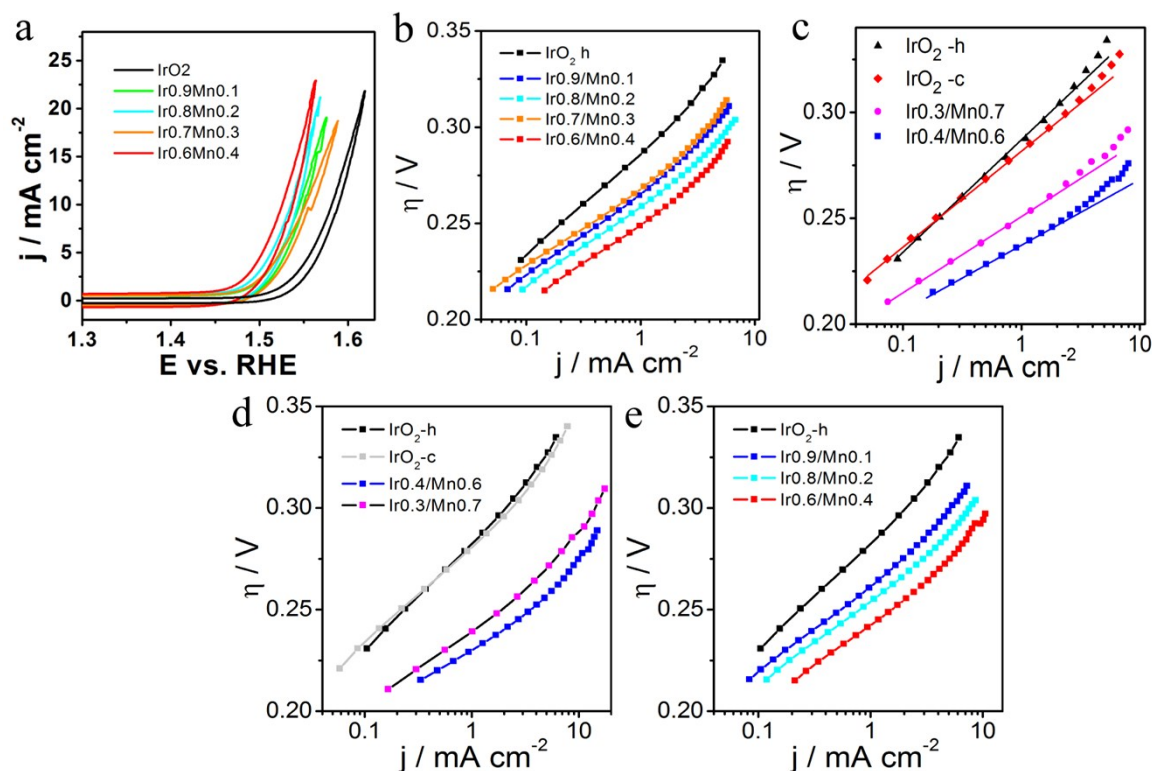
The equivalent circuit applied for fitting the impedance spectra is shown in S14a.



SUPPORTING INFORMATION

Fig S15. Electrochemical analysis of the composites.

(a) Polarization curves and (b) Tafel curves of Ir-Mn composites (Ir_{0.9}/Mn_{0.1} to Mn_{0.6}/Mn_{0.4}) and IrO₂. (c) Tafel curves of Ir_{0.4}/Mn_{0.6} and Ir_{0.3}/Mn_{0.7} composites. (d, e) The Ir loading-normalized Tafel plots for all IrO₂/MnO₂ composites. The curves in (d, e) are got by eliminating the OER current with respect to the corresponding Ir loading ratio (for IrO₂ is 0.857).



Supplementary Note S1. The mechanism of OER in acid

In acidic environments, the so-called electrochemical oxide path is described as^{4, 5}:



where M represents active metal surface site, and M-OH_{ads}, M-O_{ads} are two type adsorption intermediates. Tafel analysis is generally utilized to elucidate specific rate determining step (RDS) of surface reaction. According to the formal kinetics analysis, if step R2 representing the deprotonation of the reaction intermediate OH_{ads} controls the overall reaction rate, then for low surface coverage by intermediates OH_{ads} and O_{ads}, i.e. at low current densities, the theoretical Tafel slope (b) of 40 mV/dec is obtained. Similarly, if step R3 controls the overall reaction rate, 30 mV/dec is theoretically obtained. The Tafel slopes for IrO₂ and Ir/Mn composites, which were obtained from

SUPPORTING INFORMATION

Tafel plots, are listed in Table S3. At low current densities, the b values for homemade and commercial IrO₂ are about 56 mV/dec, in accordance with the values mentioned in the literature. However, the Ir/Mn composites show much lower slopes (in the range of 40-44 mV/dec) indicating a faster reaction pathway. The above-listed mechanism predicted from Tafel slopes reveals that the RDS for the Ir/Mn composites is deprotonation of the reaction intermediate OH_{ads}. For IrO₂ with a commonly observed b value of 60 mV/dec, the RDS is neither located at step R2 nor R3. According to the Hu group's research on the kinetics analysis of Tafel lines for IrO₂, it is assumed that step R1 is substituted by two sub-reactions:

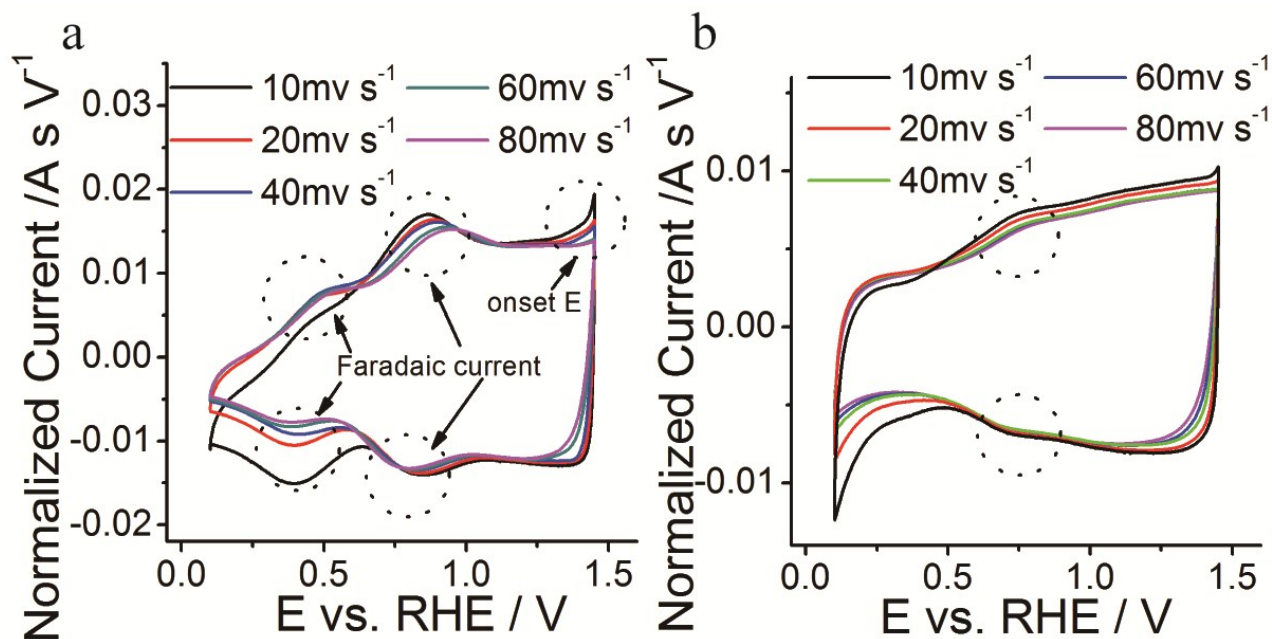


in which M-OH^{*}_{ads} and M-OH_{ads} as adsorption intermediates possess the same chemical structure, but have different energy states.⁶ In their simulation of Tafel lines with a 60 mV/dec slope, the OER is found to be completely controlled by step R1. Thus, in conclusion, the RDS for the Ir/Mn composites is different than that for IrO₂. The presence of unpaired electrons in the e_g orbitals of the Ir/Mn composites may facilitate the cleavage of the O-H bond in OH_{ads} and promote the formation of M-O_{ads} (step R2).

SUPPORTING INFORMATION

Fig S16. Normalized cyclic voltammogram curves.

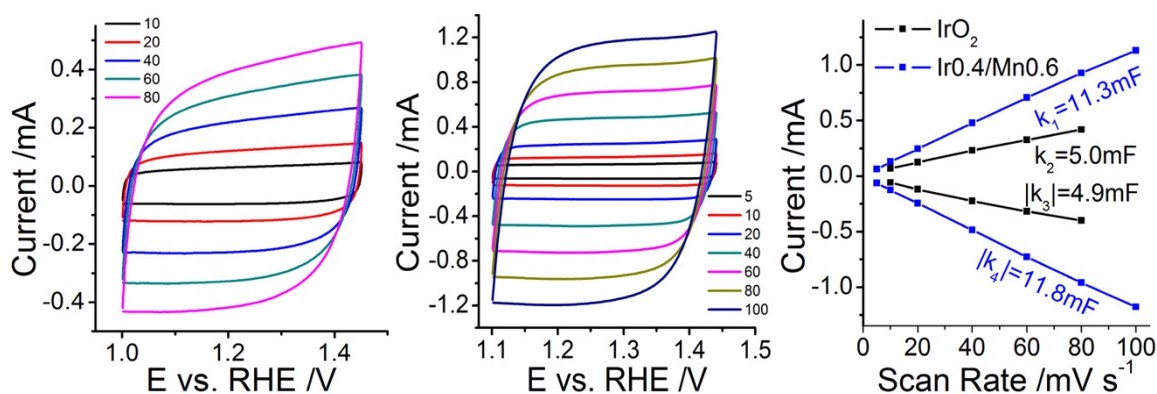
Normalized cyclic voltammogram curves (potential within 0.10V-1.45V) with different scan rates of (a) Ir_{0.4}Mn_{0.6} and (b) homemade IrO₂ in 0.1 M HClO₄. The dotted circles show the region where Faradaic currents occur, reflecting the change of metal oxidation states. The Faradaic currents at about 1.437V in (a) reveal the onset of OER.



SUPPORTING INFORMATION

Fig S17. The cyclic voltammogram curves with different scan rates.

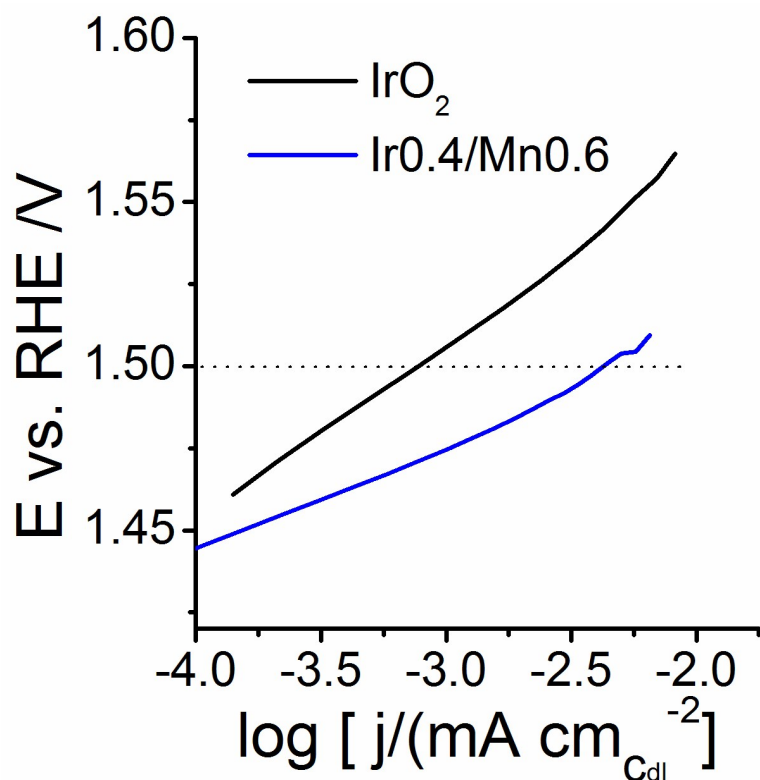
The cyclic voltammogram curves with different scan rates of (a) homemade IrO_2 and (b) $\text{Ir}_{0.4}/\text{Mn}_{0.6}$ in 0.1 M HClO_4 . For a given potential (here is 1.25V vs. RHE) where the curves are flat, slopes of the current to scan rate are plotted in (c). The current shows linear relationship with the scan rate, and absolute value of the slope is C_{dl} . The average C_{dl} for IrO_2 is 5.0 mF, and for $\text{Ir}_{0.4}/\text{Mn}_{0.6}$ is 11.6 mF. The C_{dl} determined here is similar to EIS fit results (ESI, Table S2).



SUPPORTING INFORMATION

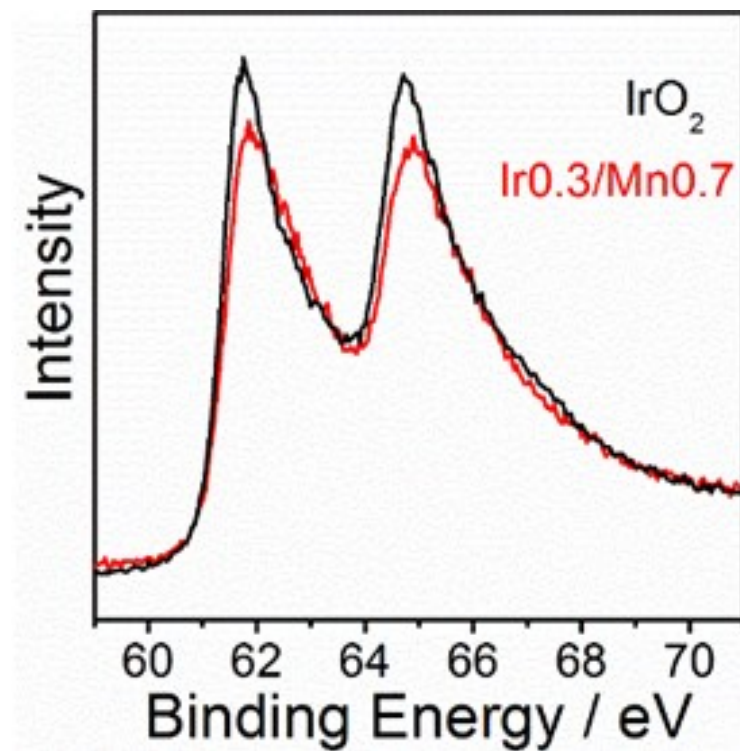
Fig S18. The oxide specific activity normalized to electrochemical surface area of Ir_{0.4}/Mn_{0.6} and IrO₂ in acidic electrolyte.

The activity is normalized to ECSA determined by C_{dl} at 1.49V (see EIS fit, Table S2). Based on this, the intrinsic activity of Ir_{0.4}/Mn_{0.6} that is 5.6 times higher than that of pure IrO₂ when normalized to electrochemical active surface area.



SUPPORTING INFORMATION

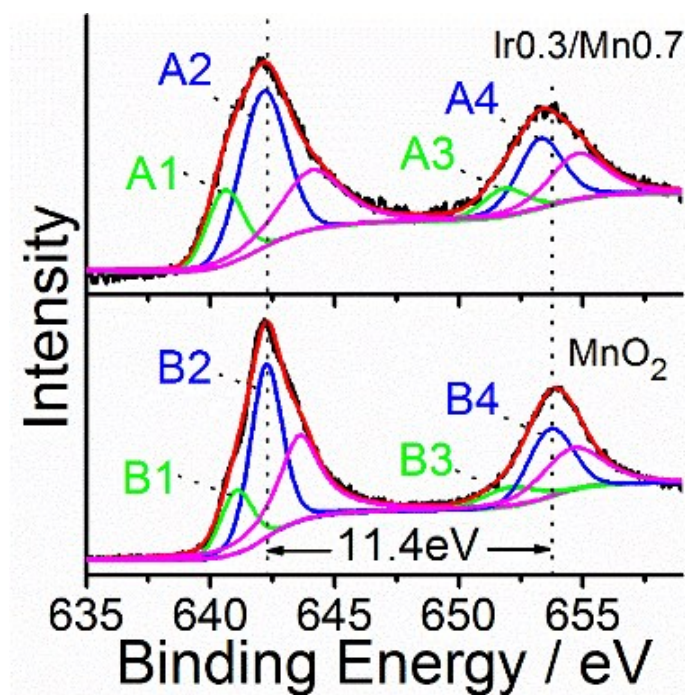
Fig S19. Comparison of the Ir 4f peak intensity of IrO₂ and Ir_{0.3}/Mn_{0.7}.



SUPPORTING INFORMATION

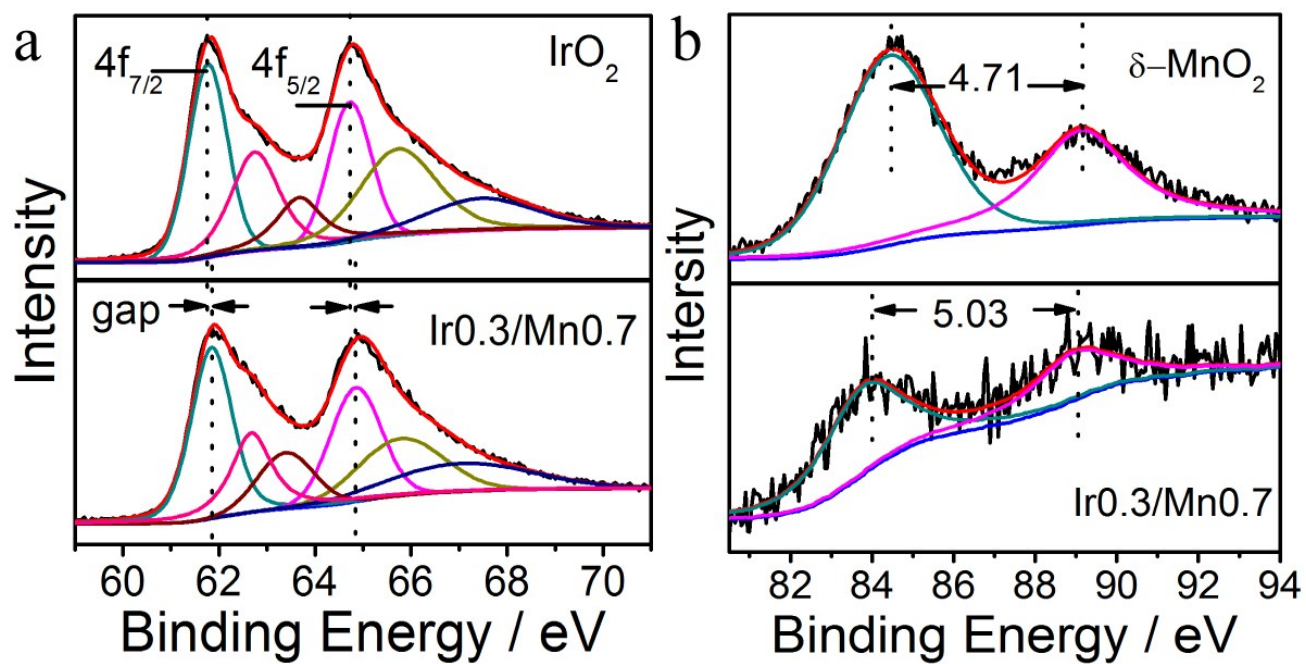
Fig S20. Mn2p spectra of Ir_{0.3}/Mn_{0.7} and δ -MnO₂.

The peaks A1, B1 at ~641.1 eV, and A3, B3 at ~651eV correspond to Mn^{III}. The peak A2, B2 at ~642.3 eV, and A4, B4 at ~654eV correspond to Mn^{IV}. A1-A2, and B1-B2 represent for the Mn 2p_{3/2} peaks, the A3-A4, B3-B4 for Mn 2p_{1/2} peaks.



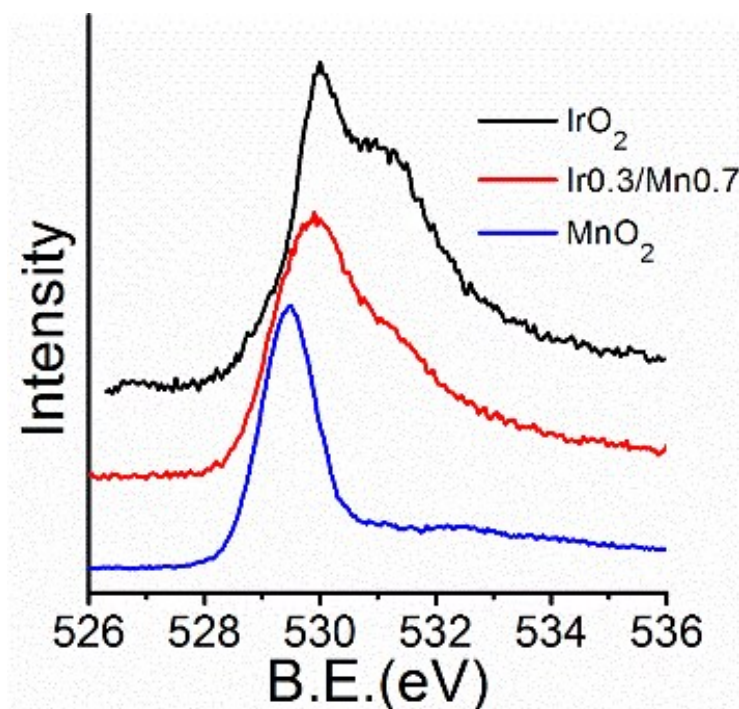
SUPPORTING INFORMATION

Fig S21. Ir4f and Mn3s spectra of Ir_{0.3}/Mn_{0.7}.



SUPPORTING INFORMATION

Fig S22. O1s XPS spectra of δ -MnO₂, IrO₂, and Ir_{0.3}/Mn_{0.7}.



Supplementary Note S2. The discussion on XPS

Figures S19–22 present typical XP spectra for the synthesized catalysts (Ir_{0.3}/Mn_{0.7}, IrO₂ and δ -MnO₂). The deconvoluted component spectra of Ir4f for Ir_{0.3}/Mn_{0.7} and IrO₂ (Fig. S19, 21) are almost the same with two symmetrical peaks at about 61.78 eV for Ir 4f_{7/2} and 64.78 eV for Ir4f_{5/2}, showing mainly the Ir⁴⁺ form. The XPS analysis of Ir_{0.3}/Mn_{0.7} and δ -MnO₂ reveals that the oxidation states of Mn are lower than 4+ form (Fig S20, 21). The spectra of O1s photoelectrons in Ir_{0.3}/Mn_{0.7} depicted in Fig. S22 consist of three components (ca. 529.3, 530.5, and 532.1 eV), which are due to the oxygen in the oxides crystal lattice (M-O, M=Metal), chemisorbed oxygen via surface hydroxyl (O⁻), and the oxygen in adsorbed water in the atmosphere (O²⁻). The oxygen energy states of Ir_{0.3}/Mn_{0.7} composite shows is between IrO₂ and MnO₂, which is middle state of the mixed oxides. This is in accordance with the catalyst structure of IrO₂ loaded MnO₂. X-ray photoemission spectrum (XPS) reveals that the composite has plenty of surface Ir^{III}, Mn^{III} and hydroxyl oxygen defects.

A reliable distinction for Mn oxidation state should be the degree of Mn-3s peak splitting that is caused primarily by the exchange interaction of non-ionized 3s electrons with 3d valence-band electrons. Generally, Mn-3s peak splitting width of about 4.5eV can be diagnosed for MnO₂, about 5.5eV for Mn₂O₃ or Mn₃O₄, and about 5.9eV for

SUPPORTING INFORMATION

MnO.^{7, 8} For δ -MnO₂, the Mn-3s splitting width is 4.7eV, revealing an oxidation state slightly lower than 4+. For Ir_{0.3}/Mn_{0.7}, the Mn-3s splitting width is higher than the δ -MnO₂, which indicates that the average Mn oxidation state has decreased and lies between +3 and +4. As for the Mn-2p spectrum (Figure S20) of δ -MnO₂, the peak B1 at 641.1 eV corresponds to Mn^{III}, and the peak B2 at 642.3 eV to Mn^{IV}. After coupling with IrO₂, the Mn-2p spectrum of Ir_{0.3}/Mn_{0.7} exhibits a significant negative shift of the peak A2, confirming a lower chemical oxidation of Mn.

SUPPORTING INFORMATION

Fig S23. The k_2 -weighted Ir-L_{III} edge EXAFS spectra.

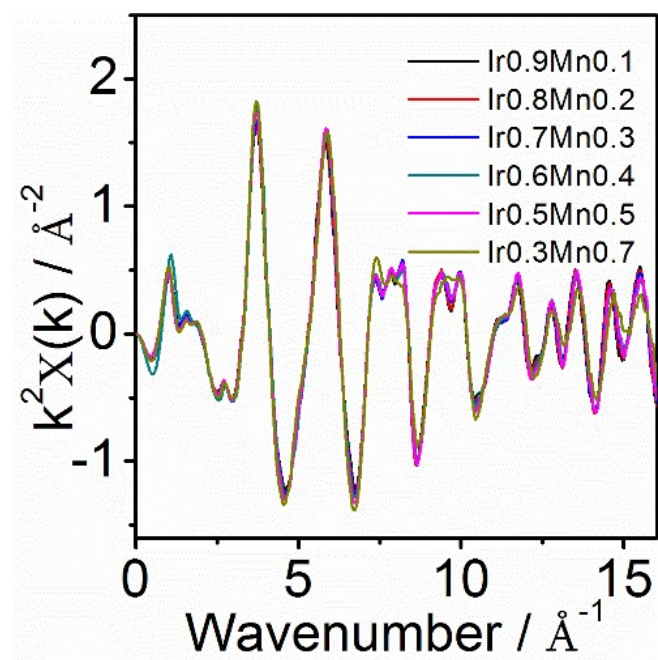
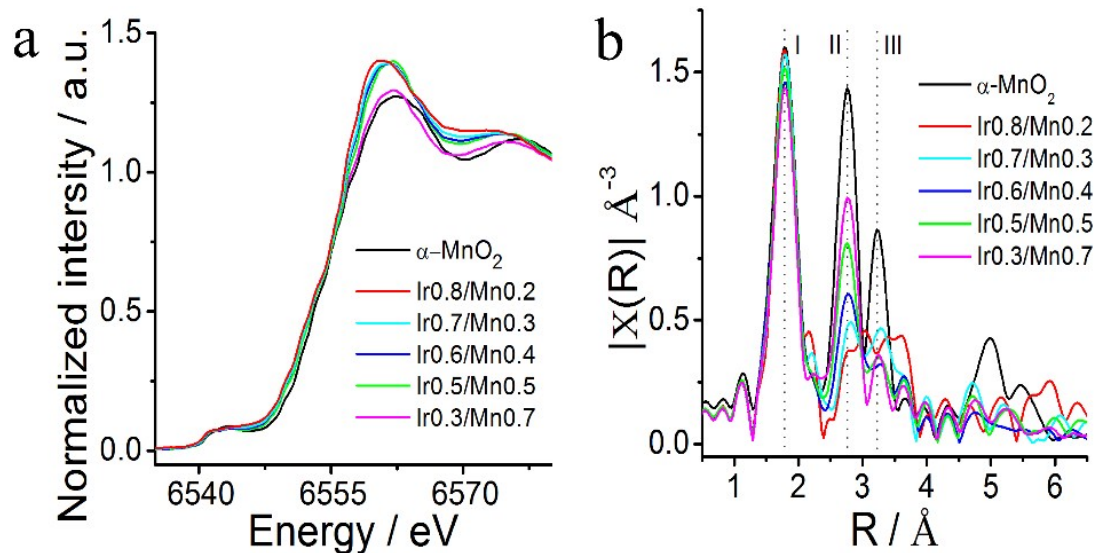


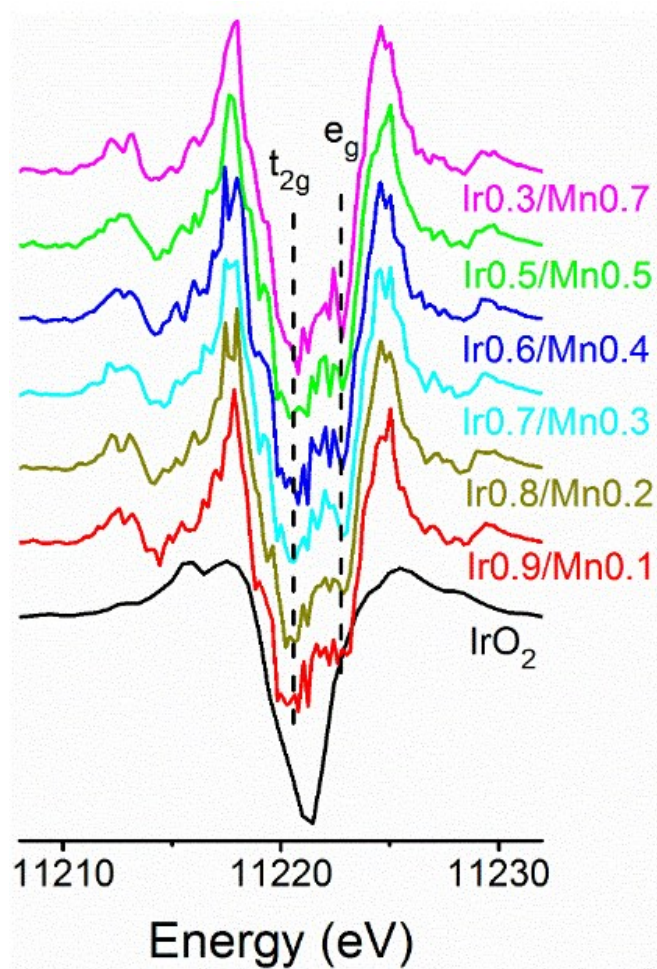
Fig S24. XAS analysis of Mn.

(a) The Mn K-edge XANES spectra for IrO₂/MnO₂ composites; (b) Fourier transforms of (a). The region I reflects the Mn-O shell, region II reflects the Mn-Mn shell, and the region III reflects the Mn-Mn shell of α -MnO₂, or one Mn-O shell of δ -MnO₂;



SUPPORTING INFORMATION

Fig S25. Second order derivative of Ir L_{III} edge of IrO_2 and Ir/Mn composites.



SUPPORTING INFORMATION

Tables

Table S1. The precursors during preparation of Ir/Mn catalysts.

Catalysts	56.7mM H₂IrCl₆	113.4 mM Mn(NO₃)₂	30% H₂O₂	1M NaOH	H₂O
	/ml	/ml	/ml	/ml	/ml
IrO₂-h	3	0	0.5	10	5
Ir0.9/Mn0.1	2.7	0.15	0.5	10	5
Ir0.8/Mn0.2	3.2	0.4	0.5	10	5
Ir0.7/Mn0.3	2.8	0.6	0.5	10	5
Ir0.6/Mn0.4	2.7	0.9	0.5	10	5
Ir0.4/Mn0.6	1.6	1.2	0.5	10	5
Ir0.3/Mn0.7	1.2	1.4	0.5	10	5

SUPPORTING INFORMATION

Table S2. EIS fit parameters for Ir/Mn composites in Fig S14.

Catalysts	R_u /ohm cm^2	R_{ct} /ohm cm^2	Y /S s^n cm^{-2}	n	$C_{\text{CPE-dl}}$ /mF cm^{-2}	C_{dl} /mF	ECSA /cm ²
IrO₂-h	6.3	5.1	0.052	0.757	27.9	5.6	159
Ir0.9/Mn0.1	6.0	4.2	0.076	0.726	40.4	8.1	231
Ir0.8/Mn0.2	5.8	4.3	0.079	0.686	37.4	7.5	214
Ir0.6/Mn0.4	6.5	4.2	0.067	0.721	33.8	6.8	193
Ir0.4/Mn0.6	6.1	2.5	0.112	0.674	51.2	10.2	293
Ir0.3/Mn0.7	6.3	4.4	0.045	0.722	19.7	3.9	113

Note: The equivalent circuit applied for fitting the impedance spectra of Ir/Mn composites is shown in Fig S14a inset. The impedance spectra of Ir/Mn samples were fitted by the so-called constant phase element (CPE) model comprising one constant phase element, with a constant phase element in parallel with a resistor. The true capacitance from this depressed semicircle model can be calculated by the following equation⁹⁻¹²:

$$C_{\text{CPE-dl}} = [Y \left(\frac{1}{R_u} + \frac{1}{R_{ct}} \right) n - 1]^{1/n} \quad (7)$$

In which C , Y , R_{ct} , R_u and n indicate the specific capacitance (F. cm^{-2}), a constant with dimension (S. s^n), ionic charge-transfer resistance (Ω . cm^2), the ohmic resistance of solution (Ω . cm^2) and a constant without dimension, respectively. Considering the impedance of a CPE is represented as $Z(\text{CPE}) = 1/((i\omega)^n Y)$ (ω is the frequency of the sinusoidal applied potential, $i = (-1)^{1/2}$), the units of Y are "S s^n cm^{-2} ".

SUPPORTING INFORMATION

Table S3. The electrochemical performance comparison of Ir_{0.4}/Mn_{0.6} against other Ir/Mn catalysts.

Catalysts	E at 10 mA cm ⁻² / V	b _{Tafel} /mV dec ⁻¹	Mass Activity at 1.500V /A g _{Ir} ⁻¹
Ir_{0.4}/Mn_{0.6}	1.516	40	66
IrO₂-c	1.573	52	3
IrO₂-h	1.586	56	3
Ir_{0.9}/Mn_{0.1}	1.548	47	8
Ir_{0.8}/Mn_{0.2}	1.539	45	11
Ir_{0.6}/Mn_{0.4}	1.532	44	21
Ir_{0.3}/Mn_{0.7}	1.522	43	34

SUPPORTING INFORMATION

Table S4. The electrochemical performance comparison of Ir_{0.4}/Mn_{0.6} against other Ir oxide-based catalysts.

Catalysts	E / V at 10 mA cm ⁻²	b _{Tafel} /mV dec ⁻¹	Mass Activity/ A g _{Ir} ⁻¹ at 1.500V	catalyst loading /mg cm ⁻²	electrolyte	ref
Ir_{0.4}/Mn_{0.6} composite	1.516	40	66	0.20	0.1M HClO ₄	This work
IrO₂-150	NG	44	10	0.10	0.1M HClO ₄	13
IrO₂-TiO₂-245	NG	42	10@1.485V	0.10	0.1M HClO ₄	14
INC-50 (Ir-Ni-Co oxide)	1.514	53	55	0.20	0.1M HClO ₄	15
IrNi_{0.57}Fe_{0.82}/C	1.513	49	56	0.09	0.5M H ₂ SO ₄	16
Ir_{0.46}Co_{0.54}O_y	1.540	59	NG	0.85	1M NaOH	17
IrOx/ATO	1.665	58	22	0.01 for Ir	0.05M H ₂ SO ₄	
Cry Mn-Ir	1.569	76	28	0.20	0.1M HClO ₄	18
Ir_{0.7}Cu_{0.3}O₅	1.580	63	7	0.20	0.1M HClO ₄	19
K_{0.25}IrO₂	1.580	65	6	0.20	0.1M HClO ₄	20
Meso-Sb-SnO₂ / IrO₂ 31wt%	1.543@ 1mA cm ⁻²	51	0 459@1.60V	0.10	0.5M H ₂ SO ₄	21
IrNiO_x@Meso- ATO-180	1.562	NG	89@1.51V	0.01 for Ir	0.05M H ₂ SO ₄	22

SUPPORTING INFORMATION

Table S5. Crystal structure change of IrO₂ in the composites simulated by Diamond software.

Catalyst	Ir-Ir length /Å	c-axis length /Å	a-axis length /Å	c/a	planar Ir-O / Å	polar Ir-O / Å
IrO ₂	3.162	3.146	4.499	0.699	1.9788	1.9800
Ir _{0.9} /Mn _{0.1}	3.142	3.126	4.506	0.694	1.9732	1.9818
Ir _{0.8} /Mn _{0.2}	3.138	3.122	4.507	0.693	1.9718	1.9823
Ir _{0.7} /Mn _{0.3}	3.129	3.113	4.511	0.690	1.9689	1.9840
Ir _{0.6} /Mn _{0.4}	3.123	3.107	4.513	0.688	1.9668	1.9849
Ir _{0.5} /Mn _{0.5}	3.120	3.104	4.514	0.688	1.9658	1.9853
Ir _{0.3} /Mn _{0.7}	3.100	3.084	4.521	0.682	1.9591	1.9884

[a] Basing on the Ir-Ir first shell distances got from Ir EXAFS, the values of c-axis length are estimated.

[b] From Ir EXAFS spectra, the distance of Ir-Ir shell near 3.55Å almost keeps unchanged. By assuming this Ir-Ir shell distance ($d_{\text{Ir-Ir}}$) remains constant, the a-axis length is calculated. The values of a, c and d have a relationship in solid geometry: $c^2 + 2a^2 = 4 d_{\text{Ir-Ir}}^2$.

Supplementary Note S3. Discussion on simulation by Diamond

To understand the effect of c-axis length reduction on the crystal structure of IrO₂, estimation is conducted with help of Diamond software. As presented in Figure 4c, d, the peaks around 3.8 Å, reflecting corner-sharing Ir-Ir shells, show negligible distance change. The distance of corner-sharing Ir-Ir atoms is a function of only c and a values. So the corner-sharing Ir-Ir distance of the composites are assumed to be same as like IrO₂. In this way, with a given value of c, the a-axis length can be calculated. The c-axis lengths of the composites are calibrated with the first Ir-Ir distance values in EXAFS and crystal parameters of IrO₂. Based on these, the values of c, a, Ir-Ir distance and Ir-O distance are estimated, as listed in Table S5. In comparison with IrO₂, the composite possessed two elongated polar Ir-O bonds, and four shortened planar Ir-O bonds (Table S5, values taken from Diamond simulation). The results conform the z-extension Jahn-Teller distortion. The corresponding powder patterns in Diamond clearly show the same trend in diffraction angle shift of (101) and (211) as has been observed in XRD.

References

1. Q. Feng, Z.-H. Liu and K. Ooi, in *Materials Syntheses: A Practical Guide*, eds. U. Schubert, N. Hüsing and R. M. Laine, Springer Vienna, Vienna, 2008, pp. 65-70.
2. J. Matthey, "PGM Market Reports", www.platinum.matthey.com/documents/new-item/pgm%20market%20reports/pgm%20market%20report%20may%202014.pdf.
3. J. Matthey, "PGM Market Reports", www.platinum.matthey.com/documents/new-item/pgm%20market%20reports/pgm_market_report_may_2017.pdf, www.platinum.matthey.com/documents/new-item/pgm%20market%20reports/pgm_market_report_may_2017.pdf.
4. J. O. M. Bockris, *The Journal of Chemical Physics*, 1956, **24**, 817-827.
5. T. Reier, H. N. Nong, D. Teschner, R. Schlogl and P. Strasser, *Advanced Energy Materials*, 2017, **7**, 1601275.
6. J.-M. Hu, J.-Q. Zhang and C.-N. Cao, *International Journal of Hydrogen Energy*, 2004, **29**, 791-797.
7. Y. Gorlin, B. Lassallekaiser, J. D. Benck, S. Gul, S. M. Webb, V. K. Yachandra, J. Yano and T. F. Jaramillo, *Journal of the American Chemical Society*, 2013, **135**, 8525-8534.
8. Z. Geng, Y. Wang, J. Liu, G. Li, L. Li, K. Huang, L. Yuan and S. Feng, *ACS Applied Materials & Interfaces*, 2016, **8**, 27825-27831.
9. G. J. Brug, A. L. G. van den Eeden, M. Sluyters-Rehbach and J. H. Sluyters, *Journal of Electroanalytical Chemistry and Interfacial Electrochemistry*, 1984, **176**, 275-295.
10. B. M. Jović, U. Č. Lačnjevac, V. D. Jović, L. Gajić-Krstajić, J. Kovač, D. Poleti and N. V. Krstajić, *International Journal of Hydrogen Energy*, 2016, **41**, 20502-20514.
11. A. J. Terezo, J. Bisquert, E. C. Pereira and G. Garciabelmonte, *Journal of Electroanalytical Chemistry*, 2001, **508**, 59-69.
12. C. C. L. McCrory, S. Jung, J. C. Peters and T. F. Jaramillo, *Journal of the American Chemical Society*, 2013, **135**, 16977-16987.
13. D. F. Abbott, D. Lebedev, K. Waltar, M. Povia, M. Nachttegaal, E. Fabbri, C. Coperet and T. J. Schmidt, *Chemistry of Materials*, 2016, **28**, 6591-6604.
14. E. Oakton, D. Lebedev, M. Povia, D. F. Abbott, E. Fabbri, A. Fedorov, M. Nachttegaal, C. Copéret and T. J. Schmidt, *ACS Catalysis*, 2017, **7**, 2346-2352.
15. W. Q. Zaman, Z. Wang, W. Sun, Z. Zhou, M. Tariq, L. Cao, X.-Q. Gong and J. Yang, *ACS Energy Letters*, 2017, **2**, 2786-2793.
16. L. Fu, G. Cheng and W. Luo, *Journal of Materials Chemistry A*, 2017, **5**, 24836-24841.
17. A. Yu, C. Lee, M. H. Kim and Y. Lee, *ACS Applied Materials & Interfaces*, 2017, **9**, 35057-35066.
18. W. Sun, L. Cao and J. Yang, *Journal of Materials Chemistry*, 2016, **4**, 12561-12570.
19. W. Sun, Y. Song, X. Gong, L. Cao and J. Yang, *Chemical Science*, 2015, **6**, 4993-4999.
20. W. Sun, Y. Song, X. Gong, L. Cao and J. Yang, *ACS Applied Materials & Interfaces*, 2016, **8**, 820-826.
21. Jinlin T. Yuan L. Qi P. Wei H. Qiong Wu, *Journal of Materials Science*, 2017, **52**, 13427-13443.
22. H. N. Nong, H. Oh, T. Reier, E. Willinger, M. G. Willinger, V. Petkov, D. Teschner and P. Strasser, *Angewandte Chemie*, 2015, **54**, 2975-2979.